NASA Technical Memorandum 4601

Comparison of Computational and Experimental Results for a Supercritical Airfoil

Melissa B. Rivers and Richard A. Wahls
Langley Research Center • Hampton, Virginia

National Aeronautics and Space Administration
Langley Research Center • Hampton, Virginia 23681-0001

November 1994

This publication is available from the following sources:

NASA Center for AeroSpace Information
800 Elkridge Landing Road
Linthicum Heights, MD 21090-2934
(301) 621-0390

National Technical Information Service (NTIS)
5285 Port Royal Road
Springfield, VA 22161-2171
(703) 487-4650

Summary

A computational investigation was performed to study the flow over a supercritical airfoil model. Solutions were obtained for steady-state transonic flow conditions using a thin-layer Navier-Stokes flow solver. The results from this computational study were compared with time-averaged experimental data obtained over a wide Reynolds number range at transonic speeds in the Langley 0.3-Meter Transonic Cryogenic Tunnel. Comparisons were made at a nominal Mach number of 0.72 and at Reynolds numbers ranging from 6×10^6 to 35×10^6.

Steady-state solutions showed the same trends as the experiment relative to shock movement as a function of the Reynolds number; the amount of shock movement, however, was overpredicted in the computations. This study demonstrates that the computational solutions can be significantly influenced by the computational treatment of the trailing-edge region of a blunt trailing-edge airfoil and the necessity of matching computational and experimental flow conditions.

Introduction

The advent of cryogenic wind tunnels has enabled simulation of full-scale flight Reynolds numbers with reasonably sized models at relatively low dynamic pressures. Among the many uses of this test technology is the basic study of two-dimensional flow over airfoils as a function of both Mach number and Reynolds number. One such study, which was conducted in the Langley 0.3-Meter Transonic Cryogenic Tunnel (0.3-m TCT), is documented in reference 1 and the wind tunnel is described in reference 2. The airfoil used in this test was a 14-percent-thick supercritical airfoil, designated as NASA SC(2)-0714, which was developed at the NASA Langley Research Center and is discussed in detail in reference 3. This airfoil had previously been tested in the 0.3-m TCT to obtain steady-flow characteristics as part of the Advanced Technology Airfoil Test (ATAT) program described in reference 4.

The experimental investigation described in reference 1, which was performed on a highly instrumented model of the SC(2)-0714 supercritical airfoil, obtained unsteady, time-dependent surface pressure measurements on an oscillating supercritical airfoil over a wide range of Reynolds numbers at transonic speeds to supplement the previous steady-flow results obtained for the nonoscillating (stationary) airfoil. During the course of the experiment, time-dependent data were also obtained for flow over the stationary airfoil.

Unsteady flow in the form of an oscillating shock was observed in the time-dependent surface pressure measurements on the stationary model. This shock movement, an unexpected result of this experimental investigation, is either a naturally occurring, flow-physics-based phenomenon for the flow over the stationary airfoil or a result of the model vibrating on its mount in the tunnel. This phenomenon provided motivation for a computational investigation in which a thin-layer Navier-Stokes flow solver is evaluated with respect to the ability to model the experimentally observed shock oscillations. The current investigation, however, is limited to the evaluation of a thin-layer Navier-Stokes flow solver with respect to the prediction of steady-state Reynolds number effects. A similar computational study of this airfoil has previously been performed by Whitlow and is discussed in reference 5.

In the present investigation, the primary objective was to assess the ability of the flow solver to predict steady-state flow over a stationary supercritical airfoil. Throughout the investigation, the effects of various computational parameters on the agreement between computation and experiment were examined. These parameters included grid trailing-edge spacing and trailing-edge closure of the computational model.

Symbols

a	speed of sound
b	airfoil span, in.
C_d	drag coefficient
C_l	sectional lift coefficient, $\frac{\text{Lift}}{\frac{1}{2}\tilde{\rho}_\infty \tilde{q}_\infty^2}$, in^{-1}
C_p	pressure coefficient, $\frac{\tilde{p} - \tilde{p}_\infty}{\frac{1}{2}\tilde{\rho}_\infty \tilde{q}_\infty^2}$
c	airfoil chord, in.
e	total energy, nondimensionalized by $\tilde{\rho}_\infty \tilde{a}_\infty^2$
G, H	inviscid fluxes
H_v	viscous fluxes
J	transformation Jacobian
L	reference length, taken as chord c, in.
M_∞	free-stream Mach number
N_{Pr}	Prandtl number, taken to be 0.72
p	pressure, nondimensionalized by $\tilde{\rho}_\infty \tilde{a}_\infty^2$
$\mathbf{Q}$	conservation variable
q	total velocity, nondimensionalized by $\tilde{a}_\infty$
$\dot{q}_{x_i}$	heat flux terms

R	Reynolds number
T	temperature, °R
t	time, nondimensionalized by $\tilde{L}/\tilde{a}_\infty$
U, V	contravariant velocities
u, v	velocities in x- and y-directions, respectively, nondimensionalized by $\tilde{a}_\infty$
u^*	shear stress velocity, $\sqrt{\tau_w/\tilde{\rho}_w}$
x, y	Cartesian coordinates, in.
y^+	wall similarity variable, $u^* y/\nu_w$
α	angle of attack, deg
γ	ratio of specific heats, taken to be 1.4
δ	Kronecker delta
η, ζ	general curvilinear coordinates
λ	coefficient of bulk viscosity
μ	coefficient of molecular viscosity
ν	kinematic viscosity, in^2/sec
ρ	density, nondimensionalized by $\tilde{\rho}_\infty$
τ_w	shear stress at wall, lb/in^2
$\tau_{x_i x_j}$	viscous shear stress terms

Abbreviations:

CFD	Computational Fluid Dynamics
Exp.	experiment
Ref.	references
TE	trailing edge

Subscripts:

i, j, k	tensor notation indices
l	lower
t	differentiation in time
u	upper
un	uncorrected
w	conditions at wall
x, y	differentiation in x- and y-directions, respectively
∞	free-stream conditions

Superscripts:

$\hat{\ }$	quantity in generalized coordinates
$\tilde{\ }$	dimensional quantity

Experimental Apparatus and Procedures

Wind Tunnel

The experimental data used in this investigation were obtained in the Langley 0.3-Meter Transonic Cryogenic Tunnel (0.3-m TCT). The 0.3-m TCT is a fan-driven, continuous-flow, transonic wind tunnel with an 8- by 24-in. two-dimensional test section. The tunnel uses cryogenic nitrogen gas as the test medium and is capable of operating at temperatures from approximately 140°R to 589°R and at stagnation pressures from approximately 1 to 6 atm with Mach number varying from approximately 0.20 to 0.90. (See ref. 2.) The ability to operate at cryogenic temperatures combined with the pressure capability of 6 atm provides a high Reynolds number capability at relatively low model loading. The floor and ceiling of the test section were slotted to reduce model blockage effects.

Model

The airfoil used in this study is the NASA SC(2)-0714, which is a 14-percent-thick phase 2 supercritical airfoil with a design lift coefficient of 0.70 and a blunt trailing edge. (See sketch A.) The design coordinates from reference 6 for this airfoil are listed in table 1. The model used in the 0.3-m TCT had a 6-in. chord, 8-in. span, and 0° sweep, and it was machined from maraging steel (fig. 1). A cavity was machined in the underside of the airfoil model to provide the space necessary to house the pressure transducers (fig. 2). This cavity was closed by a cover plate on which some lower surface transducers were mounted. The gap between the end of the airfoil and the fixed tunnel sidewall plate was sealed with a sliding seal of felt. The position of the supports was designed to locate the pitch axis at 35 percent chord. (See ref. 1 for a further description of the model details.)

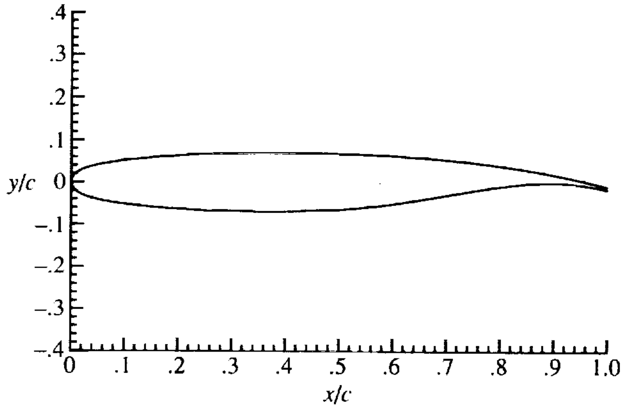

Sketch A

Instrumentation

Reference 1 also describes the instrumentation utilized for the wind tunnel test. Forty-three pressure transducers were mounted internally in the model, and the location of the transducers is shown in figure 3. Because of space constraints, 40 of the transducers were mounted in receptacles connected by a short length (nominally 0.75 in.) of tubing to the orifice. The remaining three transducers were mounted with the transducer head less than 0.1 in. below the surface of the wing. The tube-mounted transducer orifices are located alternately in two rows 0.25 in. on either side of the model midspan. On the upper surface, the orifice distribution of the 25 transducers results in an orifice every 2 percent chord from the leading edge to $x/c = 0.10$, then every 4 percent chord to $x/c = 0.70$, and finally every 5 percent chord to $x/c = 0.95$. The distribution of the 15 tube-mounted transducer orifices on the lower surface is every 2 percent chord from the leading edge to $x/c = 0.06$, and then every 10 percent chord from $x/c = 0.10$ to 0.90. Extra orifices are located at $x/c = 0.45$, 0.55, and 0.85, as described in reference 1.

The transducers were miniature, high-sensitivity, piezoresistive, differential dynamic pressure transducers with a full-scale range of 10 psid with a quoted accuracy of ± 1 percent of full-scale output. The model angle of attack was measured by an onboard accelerometer package.

Data Set

Test points were taken for this model primarily at a free-stream Mach number of 0.72, which had previously been shown (ref. 7) to be the drag rise Mach number, and at Reynolds numbers from 6×10^6 to 35×10^6. The boundary-layer transition was not fixed (through the use of grit, for example) during this experiment and all calculations in this Computational Fluid Dynamics (CFD) study were made by assuming fully turbulent flow.

The model angle-of-attack and pressure data used for this comparison were recorded directly onto analog tapes and subsequently digitized at 5000 samples/sec. The surface pressure data were then integrated to obtain the normal-force coefficient, which was assumed to be equal to the lift coefficient in reference 1 because of the small-angle approximation.

Specific data points used for the present CFD study were selected according to the desired Mach number and angle of attack. These data points were then time averaged by using the ensemble equation

$$\bar{f}(t) = \lim_{N \to \infty} \frac{1}{N} \sum_{1}^{N} f(t)$$

where $\bar{f}(t)$ is the averaged sample, $f(t)$ is the individual sample, and N is the number of samples (which varied from approximately 51 000 to 125 000, depending on the available data). These averaged data points were then integrated to produce the experimental lift coefficient needed to make angle-of-attack corrections to the original data, as discussed below.

In reference 1, experimental data for selected test conditions were corrected for wall effects; these corrections took the form of an upwash correction to the angle of attack and a blockage correction to the Mach number. The blockage corrections are presented in tabular form in reference 8 and are used in this CFD study; the corrections in reference 8 are based on the theory of reference 9. The upwash corrections described in reference 10 (sometimes referred to as the "Barnwell-Davis-Moore correction") adjust this theory with experimental data. The wall-induced downwash immediately over the model in the 0.3-m TCT is given in reference 1 as

$$\Delta\alpha = \frac{-C_l c}{8(1+j)h} \times \frac{180}{\pi}$$

The parameters necessary to make the correction are chord ($c = 6$ in.), tunnel semiheight ($h = 12$ in.), and j, where $j = aK/h$ (with a denoting a slot spacing (4 in.) and K denoting a semiempirical constant (3.2), which is a function of the slot width (0.2 in.) and the slot spacing). The values of C_l were found by integrating the time-averaged experimental pressure data and are listed in table 2. The original (uncorrected) and corrected Mach number and angle-of-attack values are also listed in table 2. Some CFD results were computed by using the corrected flow conditions, whereas others were computed by using the uncorrected flow conditions.

Computational Method

The computational method used in this study needed to have both a viscous modeling capability for the current Reynolds number effect study and a time-accurate capability for the projected follow-on studies of the experimentally observed unsteady flow. Based on these requirements, the state-of-the-art Navier-Stokes flow solver known as CFL3D was chosen. (See ref. 11.) Although CFL3D is three-dimensional and theoretically capable of solving the full Navier-Stokes equations, it is used here in its two-dimensional, thin-layer Navier-Stokes mode. The thin-layer approximation is made when the viscous terms associated with derivatives tangent to the body are considered negligible. The equations can be written in conservation form by using generalized coordinates as (see ref. 12)

$$\frac{\partial \widehat{\mathbf{Q}}}{\partial t} + \frac{\partial \widehat{G}}{\partial \eta} + \frac{\partial\left(\widehat{H} - \widehat{H}_v\right)}{\partial \zeta} = 0 \tag{1}$$

where

$$\widehat{\mathbf{Q}} = \frac{\mathbf{Q}}{J} = \frac{1}{J}\begin{bmatrix} \rho \\ \rho u \\ \rho v \\ e \end{bmatrix} \tag{2}$$

$$\widehat{G} = \frac{1}{J}\begin{bmatrix} \rho U \\ \rho U u + \eta_x p \\ \rho U v + \eta_y p \\ (e+p)U - \eta_t p \end{bmatrix} \tag{3}$$

$$\widehat{H} = \frac{1}{J}\begin{bmatrix} \rho V \\ \rho V u + \zeta_x p \\ \rho V v + \zeta_y p \\ (e+p)V - \zeta_t p \end{bmatrix} \tag{4}$$

$$\widehat{H}_v = \frac{1}{J}\begin{bmatrix} 0 \\ \zeta_x \tau_{xx} + \zeta_y \tau_{xy} \\ \zeta_x \tau_{xy} + \zeta_y \tau_{yy} \\ \zeta_x b_x + \zeta_y b_y \end{bmatrix} \tag{5}$$

$$\left.\begin{aligned} U &= \eta_x u + \eta_y v + \eta_t \\ V &= \zeta_x u + \zeta_y v + \zeta_t \end{aligned}\right\} \tag{6}$$

$$p = (\gamma - 1)\left[e - 0.5\rho\left(u^2 + v^2\right)\right] \tag{7}$$

where η is the coordinate along the body and ζ is the coordinate normal to the body. The mesh velocity is represented by the terms η_t and ζ_t. Both terms are zero for flow over a nonmoving (stationary) grid. The vector $\mathbf{Q}$ represents the density, momentum, and total energy per unit volume. The Jacobian of the transformation (J) is defined as

$$J = \frac{\partial(\eta, \zeta)}{\partial(x, y)} \tag{8}$$

The equations are nondimensionalized by the free-stream density ($\tilde{\rho}_\infty$) and speed of sound ($\tilde{a}_\infty$). The shear stress and heat flux terms are defined in tensor notation as

$$\tau_{x_i x_j} = \frac{M_\infty}{R_{\tilde{L}}}\left[\mu\left(\frac{\partial u_i}{\partial x_j} + \frac{\partial u_j}{\partial x_i}\right) + \lambda \frac{\partial u_k}{\partial x_k}\delta_{ij}\right] \tag{9}$$

$$\dot{q}_{x_i} = \left[\frac{M_\infty \mu}{R_{\tilde{L}} N_{\mathrm{Pr}}(\gamma - 1)}\right]\frac{\partial a^2}{\partial x_i} \tag{10}$$

$$\left.\begin{aligned} R_{\tilde{L}} &= \frac{\tilde{\rho}_\infty \tilde{q}_\infty \tilde{L}}{\tilde{\mu}_\infty} \\ M_\infty &= \frac{\tilde{q}_\infty}{\tilde{a}_\infty} \end{aligned}\right\} \tag{11}$$

In equation (5), the term b_{x_i} is defined in indicial notation as

$$b_{x_i} = u_j \tau_{x_i x_j} = \dot{q}_{x_i} \tag{12}$$

The hypothesis of Stokes, that is, $\lambda = -2/3\mu$, is used for bulk viscosity in equation (9), and Sutherland's law,

$$\mu = \frac{\tilde{\mu}}{\tilde{\mu}_\infty} = \left(\frac{\tilde{T}}{\tilde{T}_\infty}\right)^{3/2}\left(\frac{\tilde{T}_\infty + \tilde{c}}{\tilde{T} + \tilde{c}}\right) \tag{13}$$

is used for molecular viscosity, with $\tilde{T}_\infty$ denoting the free-stream temperature (460°R), and $\tilde{c}$ denoting Sutherland's constant (198.6°R).

An implicit, upwind-biased, finite-volume method described by Rumsey in reference 13 is used to solve equation (1). All viscous terms are centrally differenced, and implicit cross-derivative terms are neglected in this formulation. The algorithm is accurate to first order in time and to second order in space. Implicit spatial derivatives of the convective and pressure terms are first-order accurate. Because the present investigation is an upwind method, no additional artificial dissipation is necessary, and no dissipation parameters exist to be adjusted. For the entirety of this study, flux-difference splitting (that is, Roe's scheme as described in reference 14) was employed. The two-layer algebraic eddy viscosity model of Baldwin and Lomax described in reference 15 was used throughout the investigation. Additionally, a limited number of solutions were obtained using the one-half-equation turbulence model of Johnson and King (ref. 16) and the one-equation turbulence model of Baldwin and Barth (ref. 17).

Boundary conditions are applied explicitly. No-slip adiabatic wall conditions and zero pressure-gradient conditions are applied on the body to give

$$u = v = 0 \tag{14a}$$

$$\frac{\partial p}{\partial \zeta} = \frac{\partial a^2}{\partial \zeta} = 0 \tag{14b}$$

where a^2 is proportional to the fluid temperature. In the far field, the subsonic free-stream boundary conditions are determined through a characteristic analysis normal to the boundary and a point vortex representation is included for induced velocities on the outer boundary. Details can be found in reference 18 by Thomas and Salas.

Results and Discussion

Grid

As shown in sketch A, the NASA SC(2)-0714 airfoil has a blunt trailing edge. The trailing-edge thickness is 0.7 percent chord. The trailing edge was closed to facilitate the use of a single block grid, rather than rigorously modeling the blunt trailing edge with a multiblock grid; the closing of a blunt trailing edge for this purpose is a common practice and is often used successfully. (See ref. 19.) In this study, the trailing edge was initially closed by averaging the upper and lower surface trailing-edge points (fig. 4). As discussed below, initial results with this closure prompted other methods of closure to be examined; all the methods were within the framework of a single block grid.

A 257 × 65 C-mesh with 193 points on the airfoil was generated by using the GRIDGEN grid generation package. (See ref. 20.) The normal cell spacing at the surface was fixed at 1×10^{-6} chord based on the resolution requirements for turbulent flow at a chord Reynolds number of 35×10^6. The y^+ values in the cells adjacent to the surface were on the order of 1; representative values of y^+ are shown in figure 5 for low and high Reynolds numbers. As part of the airfoil closure study, the trailing-edge spacing was varied from 0.0005 to 0.012 chord. Trailing-edge grid spacing as used herein is defined as the minimum cell size tangent to and on the surface at the trailing edge. The far-field boundaries were fixed at a distance of 20 chords from the surface. Several solutions were obtained at a far-field boundary of 10 chords from the surface; comparisons of solutions for the two far-field boundary lengths showed negligible differences. Figures 6, 7, and 8 show a global, near-field, and close-up view, respectively, of a typical grid used in this study.

In addition to the baseline grid described above, two coarser grids of 129 × 33 and 65 × 17 were used to study the effects of grid density. These two coarser grids were constructed by eliminating every other point in each coordinate direction on the next finer grid. These three grids were run at a Mach number of 0.72, an angle of attack of 2°, and a chord Reynolds number of 35×10^6. Computed lift and drag coefficients are plotted in figures 9 and 10, respectively, as a function of the inverse of the mesh size (where the mesh size is equal to the total number of grid points). The lift and drag coefficients have been linearly extrapolated to values of 1.0056 and 0.0147, respectively, for a mesh of infinite density. On the finest mesh, the lift coefficient is predicted to within 1.8 percent of the extrapolated value on an infinite mesh; the drag coefficient is predicted to within 10.3 percent. Based on these results, the 257 × 65 C-mesh with 193 points on the airfoil surface was judged to be of sufficient density, and it was used throughout the remainder of the investigation.

Computational Test Conditions

All computations were made for comparison with experimental data obtained at an uncorrected Mach number of 0.72. Reynolds numbers ranged from 6×10^6 to 35×10^6 and angle of attack ranged from 0° to 2.5°. As discussed previously, Mach number and angle-of-attack corrections based on data in references 8 and 10 were evaluated and applied during the course of this study; some solutions presented below are computed at the uncorrected test conditions and others are computed at the corrected conditions. All computations were made by assuming fully turbulent flow.

Modeling Study

The initial phase of this activity involved a modeling study in which the surface smoothness, trailing-edge closure, Mach number and angle-of-attack corrections, and trailing-edge grid spacing were investigated to assess each effect prior to a detailed analysis. Because of the preliminary nature of this modeling study, the majority of the solutions in this section are not satisfactory; they serve in an academic sense showing the progression toward a satisfactory surface definition used for further study.

Wiggle. An initial solution, shown in figure 11, had a trailing-edge closure in which the upper and lower surface trailing-edge points were averaged to a single closure point. The trailing-edge grid spacing for this case is 0.008; as previously described, trailing-edge grid spacing as used herein is defined as the minimum cell size tangent to and on the surface at the trailing edge. Flow conditions used for this solution were the uncorrected Mach number of 0.72, an uncorrected angle of attack of 2°, and a Reynolds number of 35×10^6. Several aspects of this solution are of note. The first item is the oscillation on the upper surface pressure plateau. As discussed in the following paragraph, this effect was caused by a nonsmooth surface curvature d^2y/dx^2 resulting from the discrete-point geometry definition reported in reference 6.

This upper surface pressure oscillation was eliminated by smoothing the surface (defined in ref. 6) with a b-spline routine. Figures 12 and 13 show the changes in the slope and curvature, respectively, between the original and smoothed airfoil definitions. The change in the surface definition was small; the most significant surface changes occurred near the leading edge (fig. 14). The smoothed grid is defined by the same number of points as the original geometry. This smoothed geometry had a major impact on the computational results, as shown in figure 15. These computational results were obtained in the same manner as the previous results with the only change being the geometry itself. The previously computed pressure oscillations on the pressure plateau were eliminated by using this modified surface definition.

Trailing-edge closure. A second item concerning the solution in figures 11 and 15 is the spike in the pressure distribution at the trailing edge. In an attempt to improve the pressure distribution near the trailing edge, various other methods of closing the trailing edge were tried. These methods included splining the last 10 percent chord to close at the averaged trailing-edge point, extending the trailing edge until the upper and lower surfaces connected, translating the lower surface trailing-edge point to the upper surface trailing-edge point, and translating the upper surface trailing-edge point to the lower surface trailing-edge point (fig. 16). Several of these methods can result in surface discontinuities, but such approaches have previously been applied successfully (ref. 19). Figure 17 shows the computational results using the last method of trailing-edge closure with a trailing-edge spacing of 0.008 chord. This closure was judged to be the best among the four methods described above because the solution obtained from using this trailing-edge closure resulted in the best minimization of the trailing-edge spike. As discussed below, trailing-edge grid spacing also affects the results with different trailing-edge closures as it relates to the resolution of the flow around the upper surface discontinuity.

Mach number and angle-of-attack corrections. A third item of note relates to the general lack of agreement between experiment and CFD results. The discrepancies between experimental data and computational data seen in figures 11 and 15 are in large part due to the experimental Mach number and angle-of-attack corrections not being taken into account in the initial computations; therefore, corrections for Mach number and angle of attack were determined and compiled in table 2, as described previously, and have been applied for further computations. The corrected Mach number and angle of attack for the case shown in figure 15 are 0.7055 and 0.5202°, respectively. Significant improvement on the agreement between computational and experimental results is shown in figure 18. These computational runs were consistent with the original runs; only the Mach number and angle-of-attack values changed. The shock location, lower surface pressures, and pressure plateau agree much better with these corrections applied; the trailing-edge region, however, appears to need further refinement.

Trailing-edge spacing. Trailing-edge grid spacing was next examined. Figure 19 compares the original geometry definition (table 1) with a series of computational surfaces (grid) generated for trailing-edge spacings from 0.0005 to 0.012; these grids maintained a constant leading-edge spacing (tangent to and on the surface) of 0.005 and number of points on the surface. In effect, as the trailing-edge spacing changed, the change propagated over the entire chord. Note that the global effect of the change on the grid was small and that the resolution in the area of the shock was not degraded. Figure 19 shows that the smaller trailing-edge grid spacing tended to round off the discontinuity, whereas the larger trailing-edge grid spacings maintained a sharper corner. The computational results are shown in figure 20. The 0.004-chord spacing was chosen, although not optimized, and was used during the remainder of the study.

Computational Results

This section describes computed Reynolds number effects for a stationary (nonoscillating) airfoil assuming steady flow; all solutions have been computed with the Baldwin-Lomax turbulence model (ref. 15). Comparisons of Reynolds number effects with angle of attack are shown in figures 21–23. The Reynolds number range for this set of data is from 6×10^6 to 35×10^6. The corrected Mach number and angle of attack (from table 2) were used for each Reynolds number, and all cases were computed using the same grid, which had a trailing-edge spacing of 0.004 chord, a leading-edge spacing of 0.005 chord, and a normal cell spacing of 1×10^{-6} chord. As shown in figure 5, y^+ values ranged from approximately 0.5 for the Reynolds number case of 6×10^6 chord to 1.5 for the Reynolds number case of 35×10^6 chord; because of this small effect on the turbulent boundary-layer resolution (i.e., laminar sublayer) close to the surface, the same grid was used for all Reynolds numbers. Figure 21 shows the Reynolds number effects for a Mach number of 0.72 and an angle of attack of 1°; appropriate Mach number and angle-of-attack corrections (listed in table 2) have been applied in determining the conditions to obtain the computational solutions. At this low angle of attack, Reynolds number effects are difficult to discern for both the experimental and computational data.

Figure 22 shows the Reynolds number effects for a Mach number of 0.72 and an angle of attack of 2°, again with the appropriate Mach number and angle-of-attack corrections applied. The Reynolds number range for this set of data is also from 6×10^6 to 35×10^6. The Mach number and angle-of-attack corrections were again different for each Reynolds number, and all these cases were again computed by using the same grid. At this angle of attack, the shock moves aft as the Reynolds number increases for both the experimental data and computational solutions. Although the experiment and computation show the same trend (direction of shock movement), the results indicate that the shock-movement dependency to the Reynolds number was larger from computational data than from experimental data.

Figure 23 shows the Reynolds number effects for a Mach number of 0.72 and an angle of attack of 2.5°, again with appropriate Mach number and angle-of-attack corrections applied. The Reynolds number range for this angle of attack is from 6×10^6 to 30×10^6. At this angle of attack, aft movement of the shock as the Reynolds number increases is again observed for both the experimental data and computational solutions. However, similar to the previous results (see fig. 22), the shock location appears to have been predicted farther upstream compared with the experimental data, especially for the lower Reynolds number conditions.

Concluding Remarks

The purpose of this study was to determine the capability of a state-of-the-art, upwind, thin-layer Navier-Stokes flow solver to predict steady-state Reynolds number effects for flow over a two-dimensional supercritical airfoil. The study demonstrated that the computational solutions could be significantly influenced by the computational treatment of the trailing-edge region of a blunt trailing-edge airfoil. The study also demonstrated the necessity of matching computational and experimental flow conditions. Mach number and angle-of-attack corrections taken from previous documentation were assumed to be correct; these corrections improved comparisons, but modifications to these corrections may have improved comparisons further. Steady-state solutions showed the same trends as the experiment relative to shock movement as a function of the Reynolds number; however, shock location was predicted farther upstream, especially for the lower Reynolds number conditions.

NASA Langley Research Center
Hampton, VA 23681-0001
September 27, 1994

References

1. Hess, Robert W.; Seidel, David A.; Igoe, William B.; and Lawing, Pierce L.: Transonic Unsteady Pressure Measurements on a Supercritical Airfoil at High Reynolds Numbers. *J. Aircr.*, vol. 26, July 1989, pp. 605–614.
2. Ray, E. J.; Ladson, C. L.; Adcock, J. B.; Lawing, P. L.; and Hall, R. M.: *Review of Design and Operational Characteristics of the 0.3-Meter Transonic Cryogenic Tunnel.* NASA TM-80123, 1979.
3. Harris, Charles D.: *Aerodynamic Characteristics of a 14-Percent-Thick NASA Supercritical Airfoil Designed for a Normal-Force Coefficient of 0.7.* NASA TM X-72712, 1975.
4. Jenkins, Renaldo V.; Hill, Acquilla S.; and Ray, Edward J.: *Aerodynamic Performance and Pressure Distributions for a NASA SC(2)-0714 Airfoil Tested in the Langley 0.3-Meter Transonic Cryogenic Tunnel.* NASA TM-4044, 1988.
5. Whitlow, Woodrow, Jr.: *Application of Unsteady Aerodynamic Methods for Transonic Aeroelastic Analysis.* NASA TM-100665, 1988.
6. Harris, Charles D.: *NASA Supercritical Airfoils—A Matrix of Family-Related Airfoils.* NASA TP-2969, 1990.
7. Jenkins, Renaldo V.: *NASA SC(2)-0714 Airfoil Data Corrected for Sidewall Boundary-Layer Effects in the Langley 0.3-Meter Transonic Cryogenic Tunnel.* NASA TP-2890, 1989.
8. Jenkins, Renaldo V.; and Adcock, Jerry B.: *Tables for Correcting Airfoil Data Obtained in the Langley 0.3-Meter Transonic Cryogenic Tunnel for Sidewall Boundary Layer Effects.* NASA TM-87723, 1986.
9. Sewall, William G.: The Effects of Sidewall Boundary Layers in Two-Dimensional Subsonic and Transonic Wind Tunnels. *AIAA J.*, vol. 20, no. 9, Sept. 1982, pp. 1253–1256.
10. Barnwell, Richard W.: *Design and Performance Evaluation of Slotted Walls for Two-Dimensional Wind Tunnels.* NASA TM-78648, 1978.
11. Thomas, J. L.: Navier-Stokes Computations of Vortical Flows Over Low Aspect Ratio Wings. AIAA-87-0207, Jan. 1987.

12. Rumsey, Christopher L.; and Anderson, W. Kyle: Parametric Study of Grid Size, Time Step and Turbulence Modeling on Navier-Stokes Computations Over Airfoils. *Validation of Computational Fluid Dynamics. Volume 1—Symposium Papers and Round Table Discussion,* AGARD-CP-437-VOL-1, Dec. 1988. (Available from DTIC as AD-A211 893.)

13. Rumsey, C. L.: Time-Dependent Navier-Stokes Computations of Separated Flows Over Airfoils. AIAA-85-1684, July 1985.

14. Roe, P. L.: Approximate Riemann Solvers, Parameter Vectors, and Difference Schemes. *J. Comput. Phys.*, vol. 43, no. 2, Oct. 1981, pp. 357–372.

15. Baldwin, Barrett; and Lomax, Harvard: Thin-Layer Approximation and Algebraic Model for Separated Turbulent Flows. AIAA-78-257, Jan. 1978.

16. Johnson, D. A.; and King, L. S.: A Mathematically Simple Turbulence Closure Model for Attached and Separated Turbulent Boundary Layers. *AIAA J.*, vol. 23, no. 11, Nov. 1985, pp. 1684–1692.

17. Baldwin, Barrett S.; and Barth, Timothy J.: *A One-Equation Turbulence Transport Model for High Reynolds Number Wall-Bounded Flows.* NASA TM-102847, 1990.

18. Thomas, James L.; and Salas, M. D.: Far-Field Boundary Conditions for Transonic Lifting Solutions to the Euler Equations. AIAA-85-0020, Jan. 1985.

19. Londenberg, W. K.: Turbulence Model Evaluation for the Prediction of Flows Over a Supercritical Airfoil With Deflected Aileron at High Reynolds Number. AIAA-93-0191, Jan. 1993.

20. Steinbrenner, John P.; and Chawner, John R.: *The GRIDGEN Version 8 Multiple Block Grid Generation Software.* MDA Engineering Report 92-01, 1992.

Table 1. Original Design Coordinates of the NASA SC(2)-0714 Airfoil

x/c	$(y/c)_u$	$(y/c)_l$
0.000	0.000	0.000
0.002	0.01077	−0.01077
0.005	0.01658	−0.01658
0.010	0.02240	−0.02240
0.020	0.02960	−0.02960
0.030	0.03460	−0.03450
0.040	0.03830	−0.03820
0.050	0.04140	−0.04130
0.060	0.04400	−0.04390
0.070	0.04630	−0.04620
0.080	0.04840	−0.04830
0.090	0.05020	−0.05010
0.100	0.05190	−0.05180
0.110	0.05350	−0.05340
0.120	0.05490	−0.05490
0.130	0.05620	−0.05620
0.140	0.05740	−0.05740
0.150	0.05860	−0.05860
0.160	0.05970	−0.05970
0.170	0.06070	−0.06070
0.180	0.06160	−0.06160
0.190	0.06250	−0.06250
0.200	0.06330	−0.06330
0.210	0.06410	−0.06410
0.220	0.06480	−0.06480
0.230	0.06540	−0.06550
0.240	0.06600	−0.06610
0.250	0.06650	−0.06670
0.260	0.06700	−0.06720
0.270	0.06750	−0.06770
0.280	0.06790	−0.06810
0.290	0.06830	−0.06850
0.300	0.06860	−0.06880
0.310	0.06890	−0.06910
0.320	0.06920	−0.06930
0.330	0.06940	−0.06950
0.340	0.06960	−0.06960
0.350	0.06970	−0.06970
0.360	0.06980	−0.06970
0.370	0.06990	−0.06970
0.380	0.06990	−0.06960
0.390	0.06990	−0.06950
0.400	0.06990	−0.06930
0.410	0.06980	−0.06910
0.420	0.06970	−0.06880
0.430	0.06960	−0.06850
0.440	0.06950	−0.06810
0.450	0.06930	−0.06770
0.460	0.06910	−0.06720
0.470	0.06890	−0.06670
0.480	0.06860	−0.06610
0.490	0.06830	−0.06540
0.500	0.06800	−0.06460
0.510	0.06760	−0.06370
0.520	0.06720	−0.06270
0.530	0.06680	−0.06160
0.540	0.06630	−0.06040
0.550	0.06580	−0.05910
0.560	0.06530	−0.05770
0.570	0.06470	−0.05620
0.580	0.06410	−0.05460
0.590	0.06350	−0.05290
0.600	0.06280	−0.05110
0.610	0.06210	−0.04920
0.620	0.06130	−0.04730
0.630	0.06050	−0.04530
0.640	0.05970	−0.04330
0.650	0.05880	−0.04120
0.660	0.05790	−0.03910
0.670	0.05690	−0.03700
0.680	0.05590	−0.03480
0.690	0.05480	−0.03260
0.700	0.05370	−0.03040
0.710	0.05250	−0.02820
0.720	0.05130	−0.02600
0.730	0.05000	−0.02380
0.740	0.04870	−0.02160
0.750	0.04730	−0.01940
0.760	0.04580	−0.01730
0.770	0.04430	−0.01520
0.780	0.04270	−0.01320
0.790	0.04110	−0.01130
0.800	0.03940	−0.00950
0.810	0.03760	−0.00790
0.820	0.03580	−0.00640
0.830	0.03390	−0.00500
0.840	0.03190	−0.00380
0.850	0.02990	−0.00280
0.860	0.02780	−0.00200
0.870	0.02560	−0.00140
0.880	0.02340	−0.00100
0.890	0.02110	−0.00080
0.900	0.01870	−0.00090
0.910	0.01620	−0.00120
0.920	0.01370	−0.00170
0.930	0.01110	−0.00250
0.940	0.00840	−0.00360
0.950	0.00560	−0.00500
0.960	0.00270	−0.00670
0.970	−0.00020	−0.00870
0.980	−0.00320	−0.01100
0.990	−0.00630	−0.01360
1.000	−0.00950	−0.01650

Table 2. Uncorrected and Corrected Values of Mach Number and Angle of Attack

R_c	Calculated C_l	Uncorrected		Corrected	
		Mach number	Angle of attack, deg	Mach number	Angle of attack, deg
6×10^6	0.6593	0.72	1	0.701	−0.1424
10	.7328			.703	−.2698
15	.6957			.704	−.2055
30	.7364			.705	−.2760
35	.6818		↓	.7055	−.1813
6	.8482		2	.701	.5303
10	.9139			.703	.4165
15	.8201			.704	.5789
35	.8540		↓	.7055	.5202
6	.9524		2.5	.701	.8497
15	.9854			.704	.7926
30	.9834	↓	↓	.705	.7960

ORIGINAL PAGE
BLACK AND WHITE PHOTOGRAPH

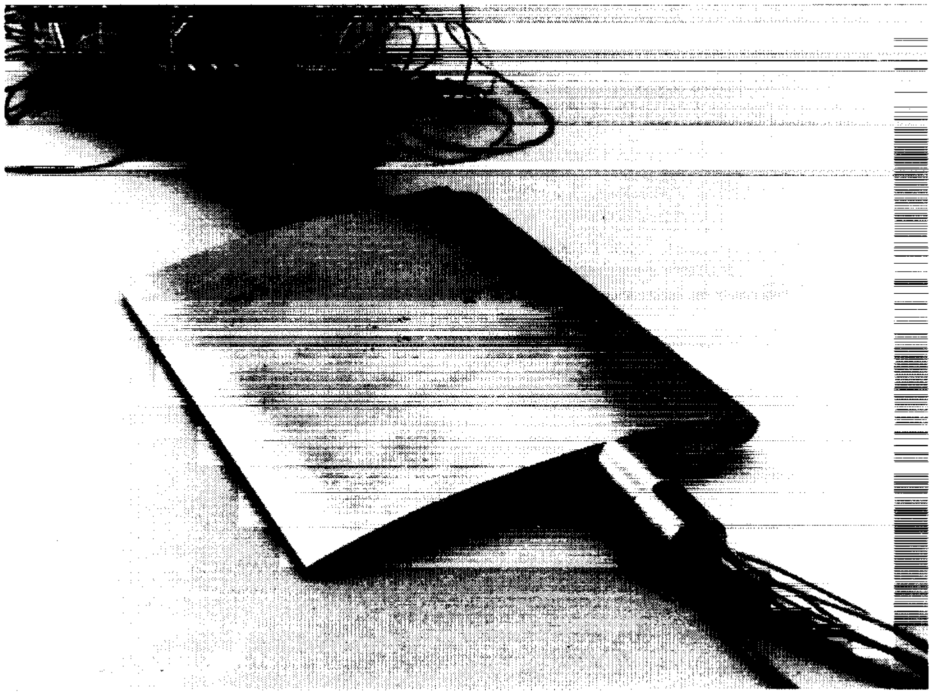

L-84-8257

Figure 1. External view of model.

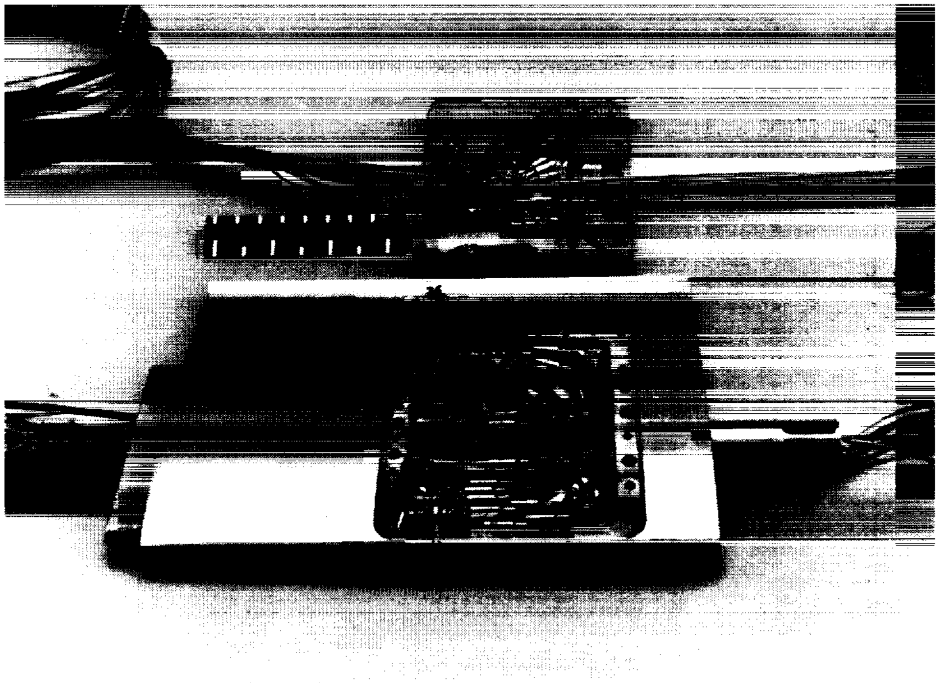

L-84-8258

Figure 2. Internal view of model.

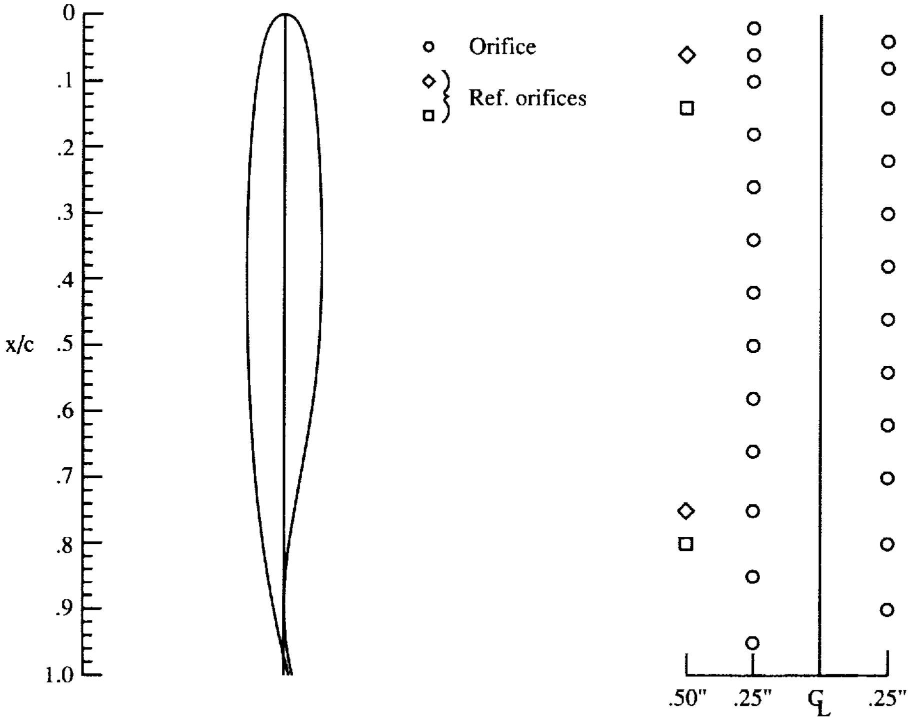
0
.1
.2
.3
.4
x/c .5
.6
.7
.8
.9
1.0
○ Orifice
◇ □ Ref. orifices
.50"
.25"
℄
.25"

(a) Upper surface.

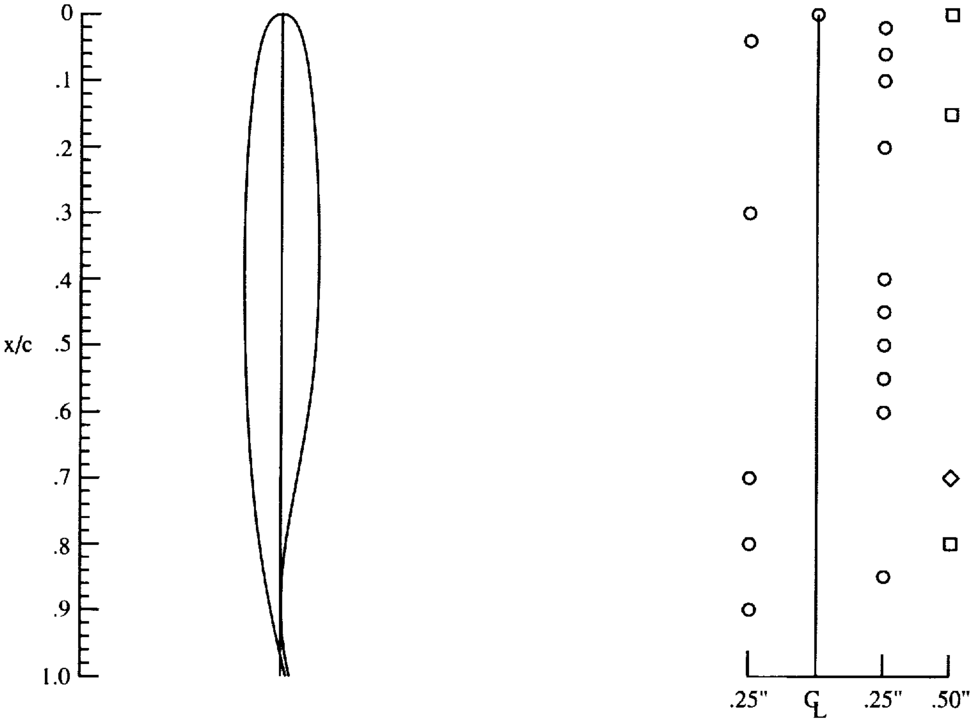
0
.1
.2
.3
.4
x/c .5
.6
.7
.8
.9
1.0
.25"
℄
.25"
.50"

(b) Lower surface.

Figure 3. Locations of transducer orifices.

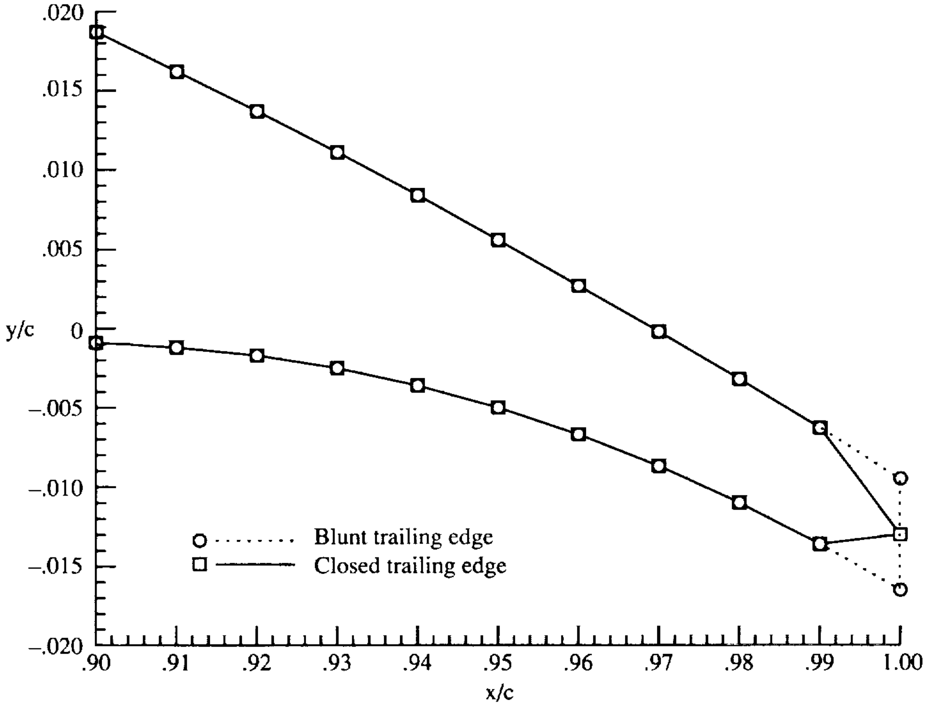

Figure 4. Trailing-edge closure modeling.

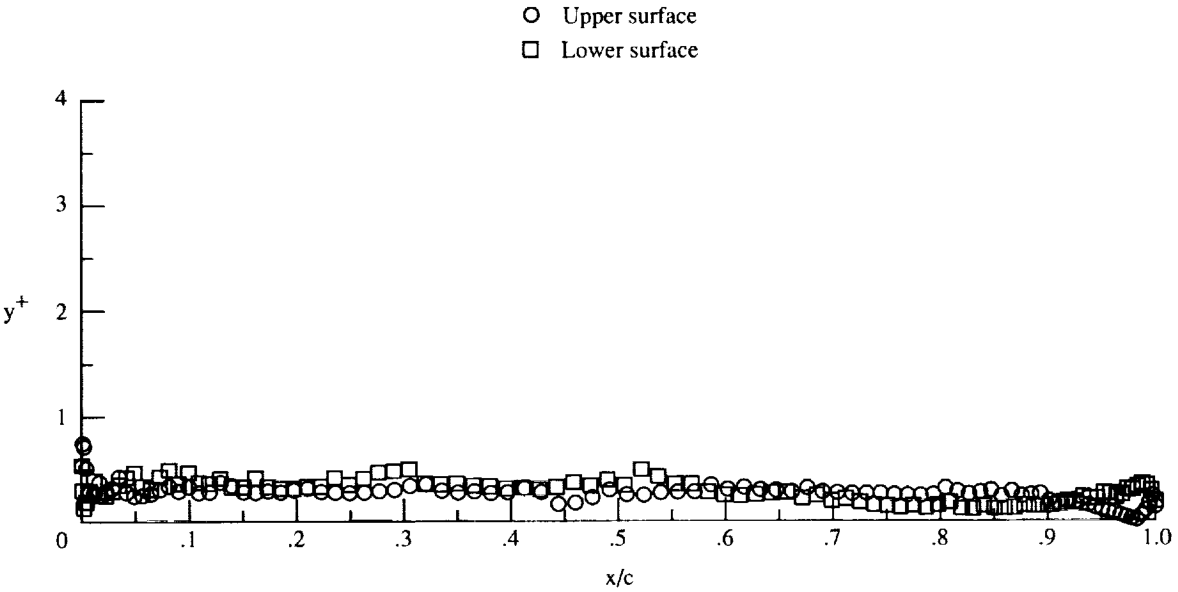

(a) $R_c = 6 \times 10^6$; $\alpha_{\text{un}} = 2.5°$.

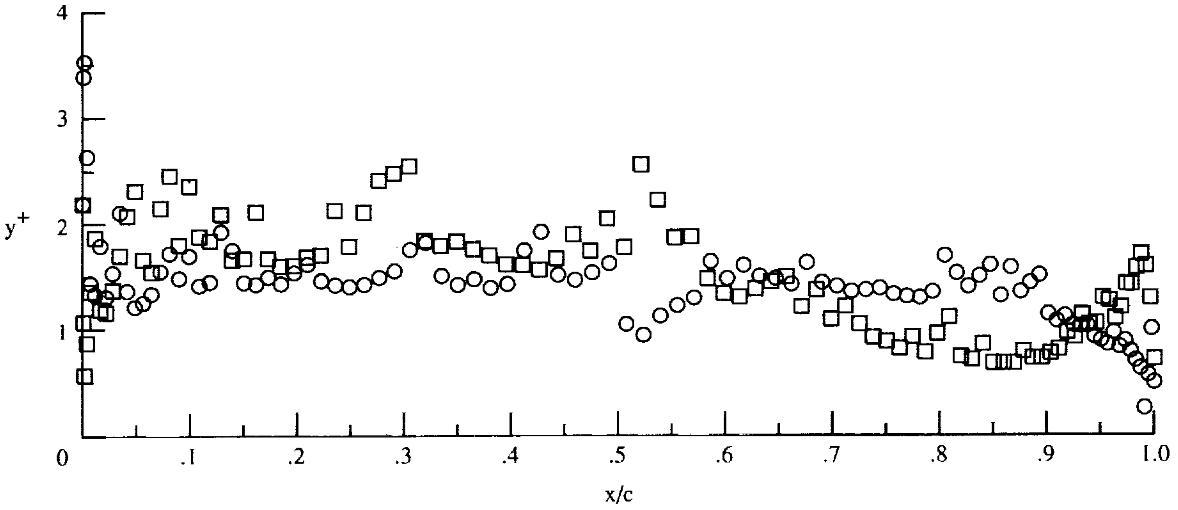

(b) $R_c = 35 \times 10^6$; $\alpha_{\text{un}} = 2°$.

Figure 5. Grid characteristics at $M_{\infty,\text{un}} = 0.72$.

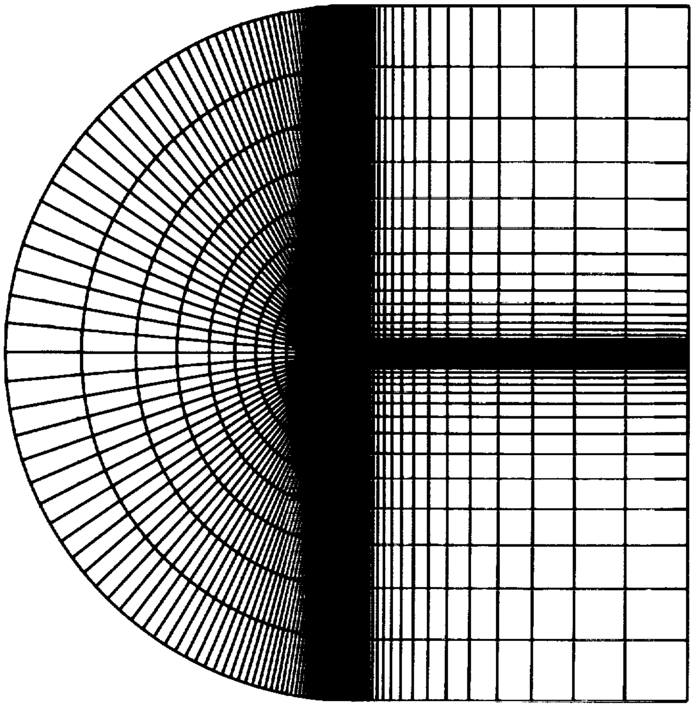

Figure 6. Global view of computational grid.

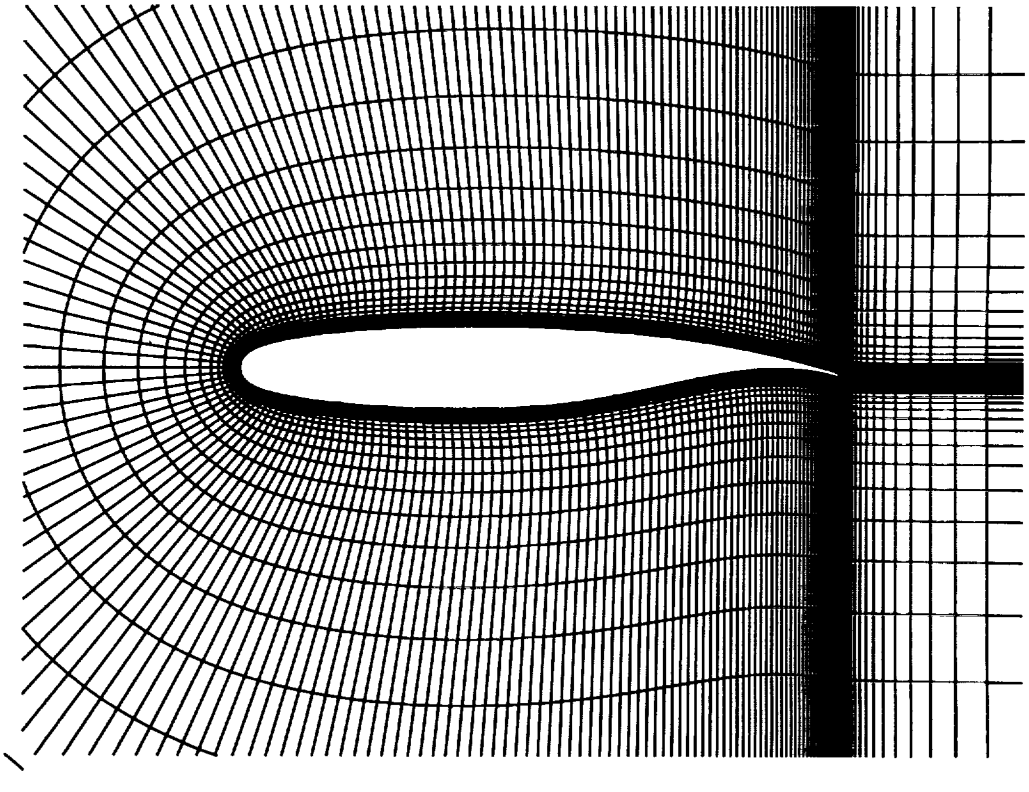

Figure 7. Near-field view of computational grid.

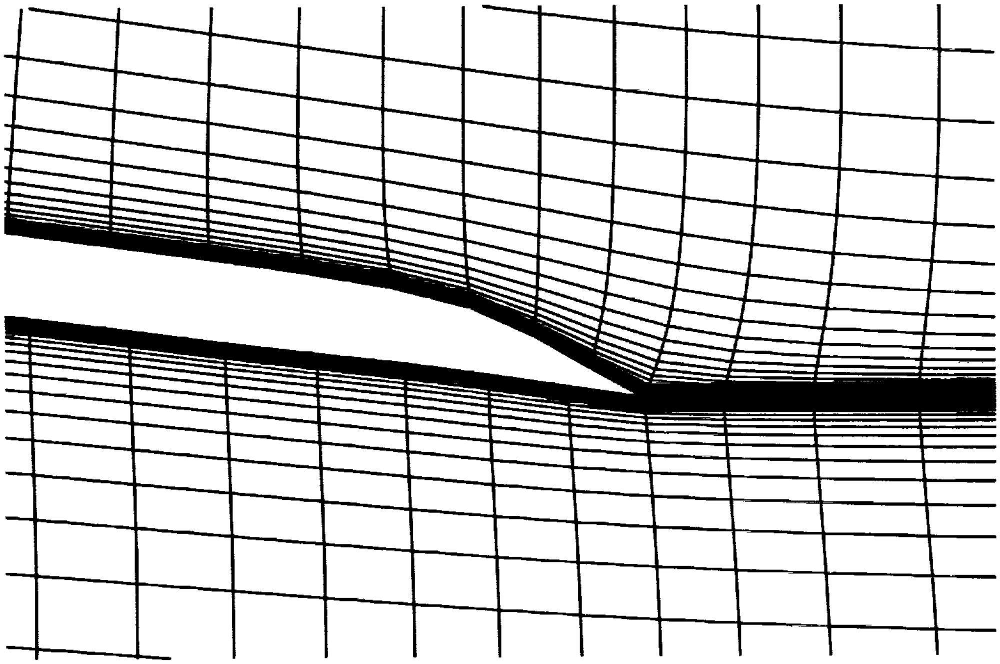

Figure 8. Close-up view of trailing edge of computational grid.

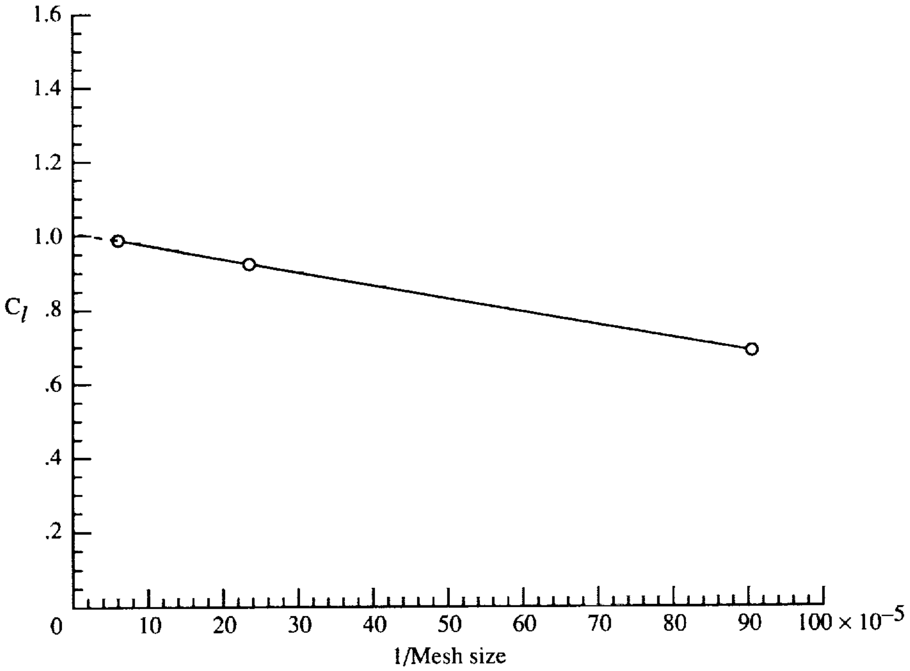

Figure 9. Grid density study showing computed lift coefficient plotted against the inverse of mesh size. $R_c = 35 \times 10^6$; $M_{\infty,\mathrm{un}} = 0.72$; $\alpha_{\mathrm{un}} = 2°$. Dashed line indicates extrapolated data.

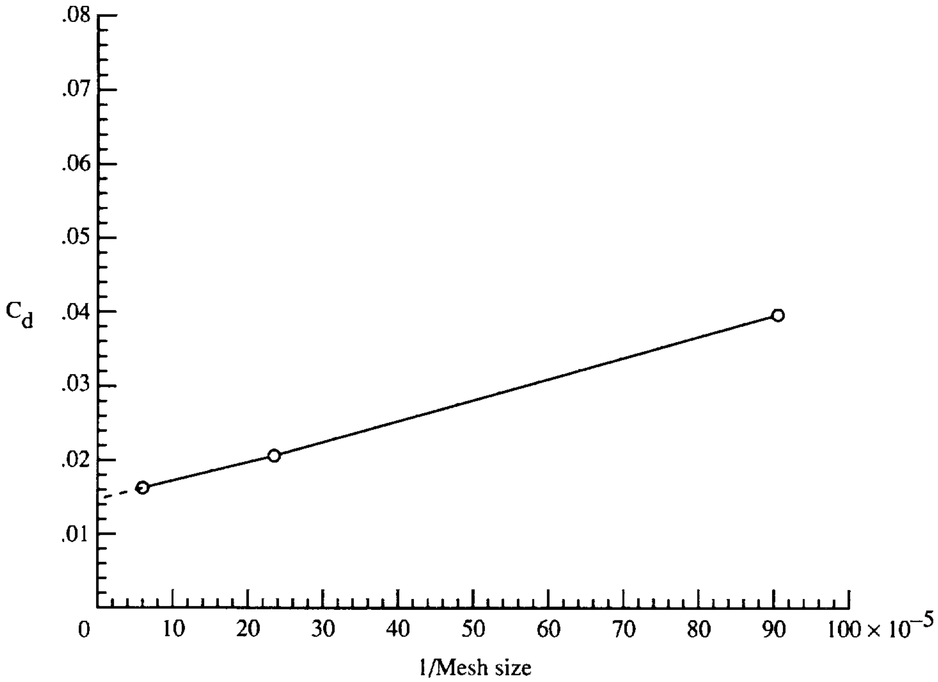

Figure 10. Grid density study showing computed drag coefficient plotted against the inverse of mesh size. $R_c = 35 \times 10^6$; $M_{\infty,\text{un}} = 0.72$; $\alpha_{\text{un}} = 2°$. Dashed line indicates extrapolated data.

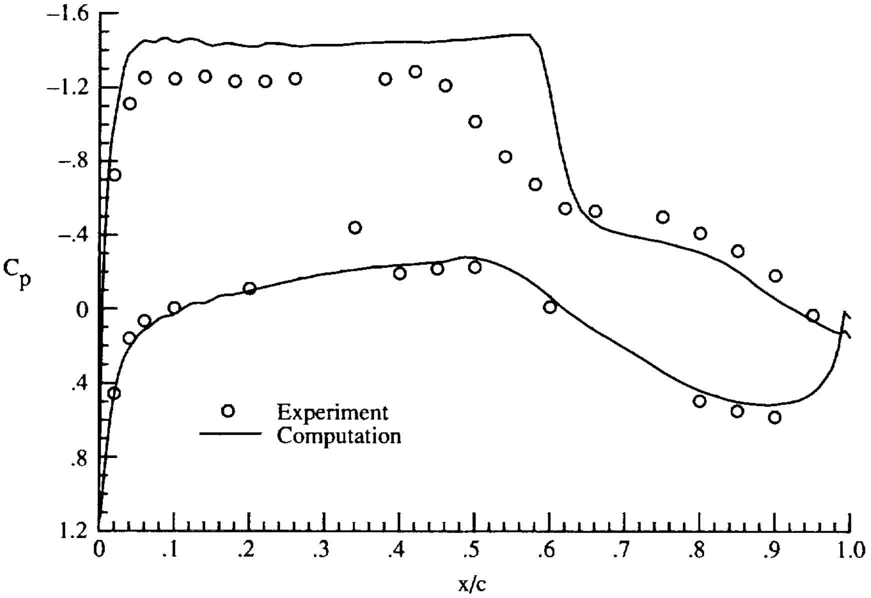

Figure 11. Initial computational result using original airfoil definition (table 1). $R_c = 35 \times 10^6$; $M_{\infty,\text{un}} = 0.72$; $\alpha_{\text{un}} = 2°$.

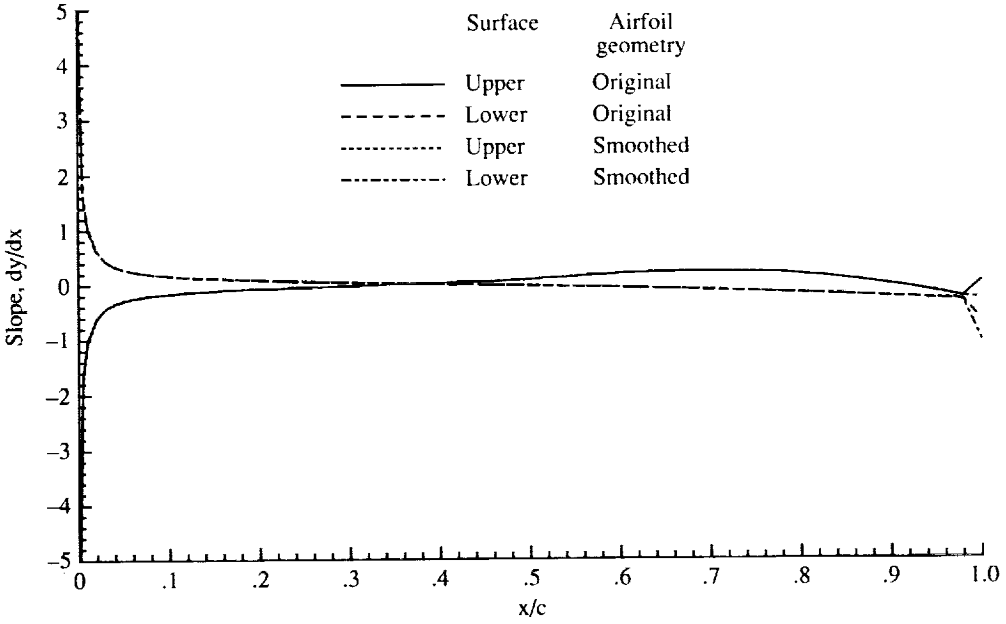

Figure 12. Change in slope between original and smoothed airfoils.

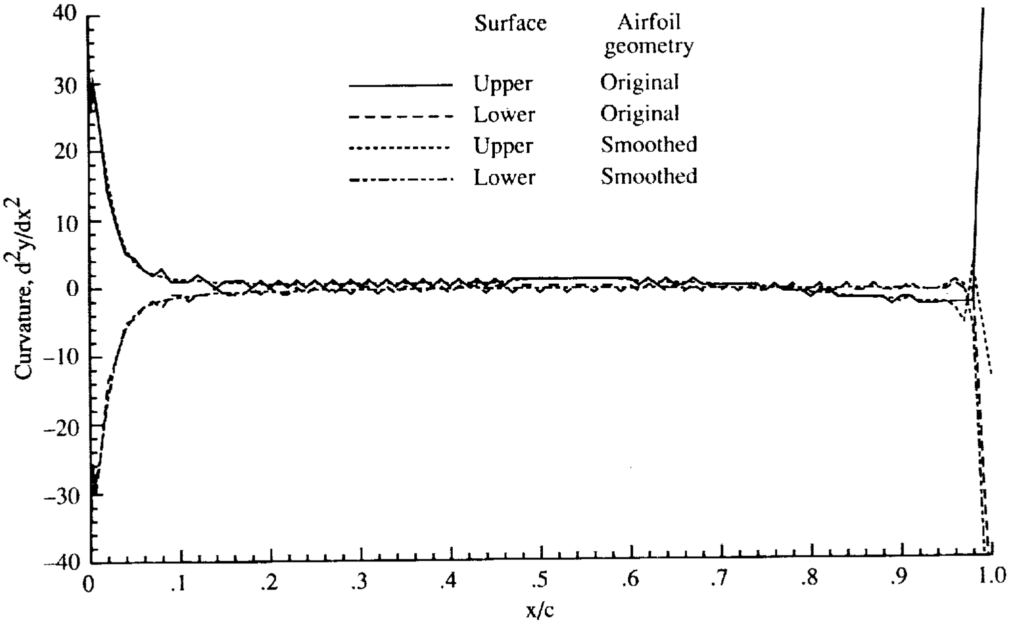

Figure 13. Change in curvature between original and smoothed airfoils.

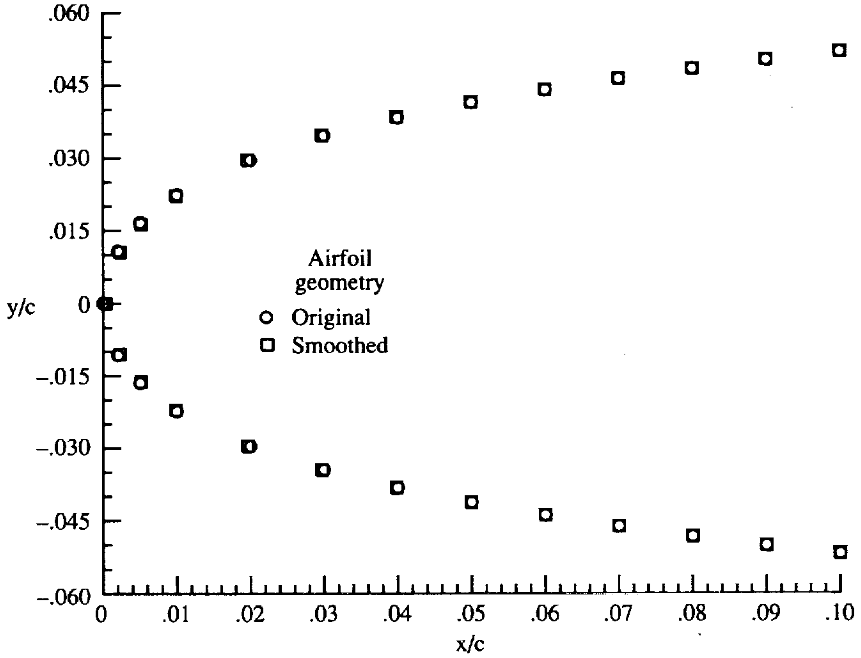

Figure 14. Smoothed airfoil geometry showing surface change near leading edge.

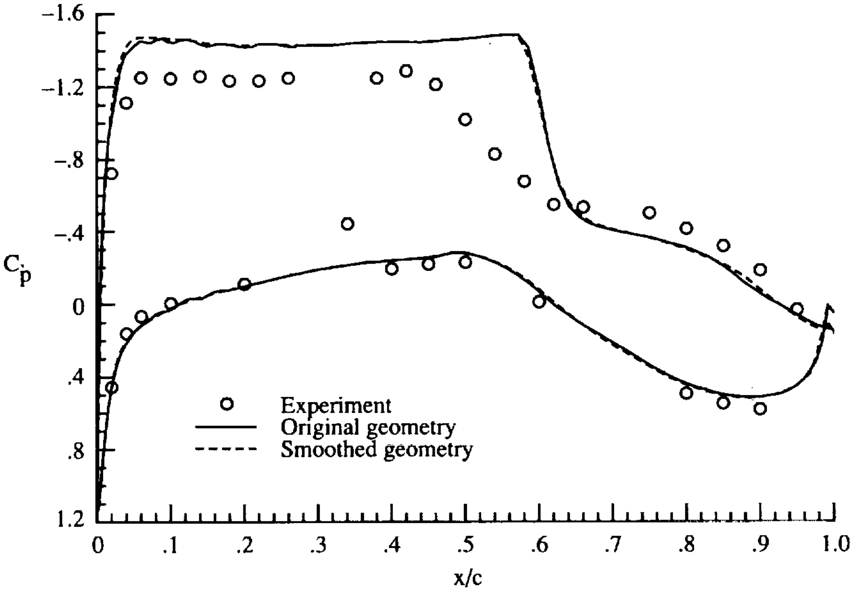

Figure 15. Effect of smoothing airfoil geometry on computational results. $R_c = 35 \times 10^6$; $M_{\infty,\mathrm{un}} = 0.72$; $\alpha_{\mathrm{un}} = 2°$.

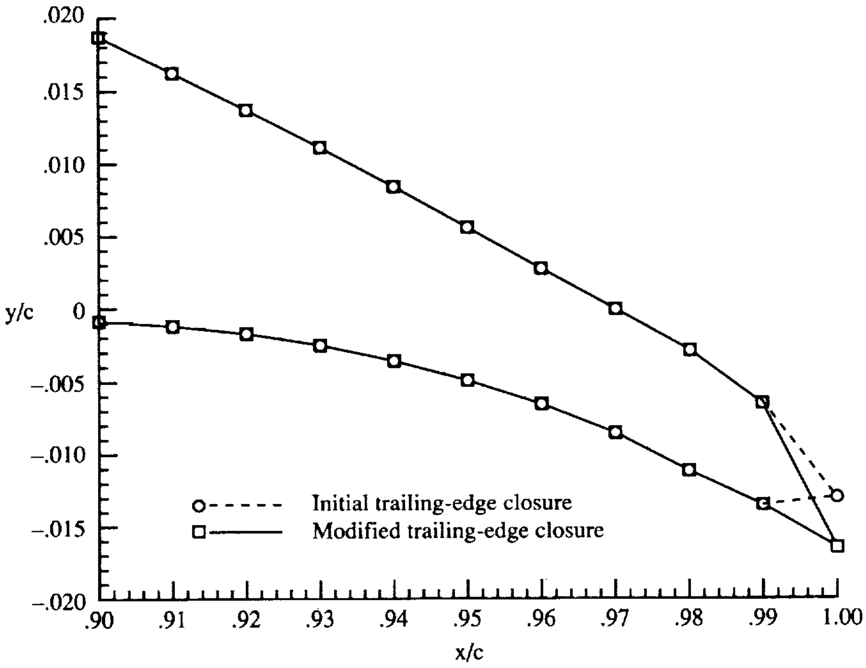

Figure 16. Modified trailing-edge closure.

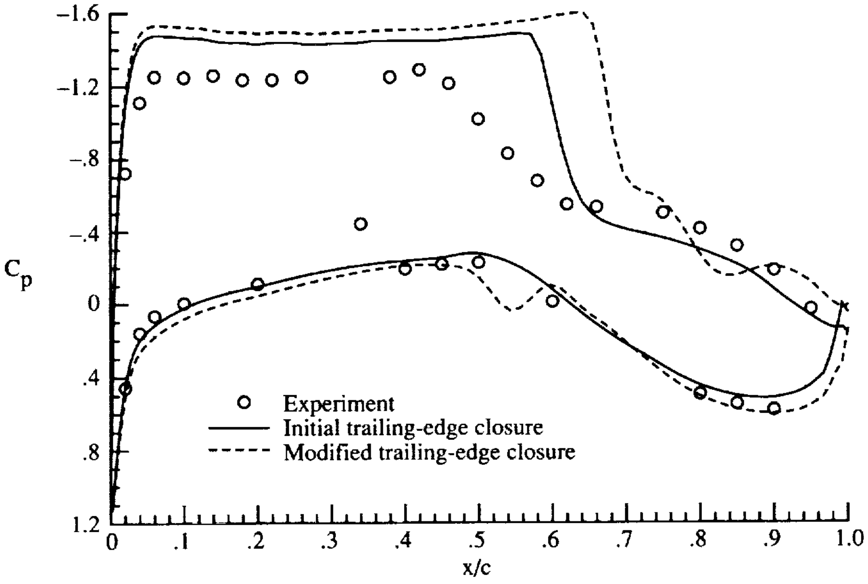

Figure 17. Effect of modified trailing-edge closure. $R_c = 35 \times 10^6$; $M_{\infty,\text{un}} = 0.72$; $\alpha_{\text{un}} = 2^\circ$.

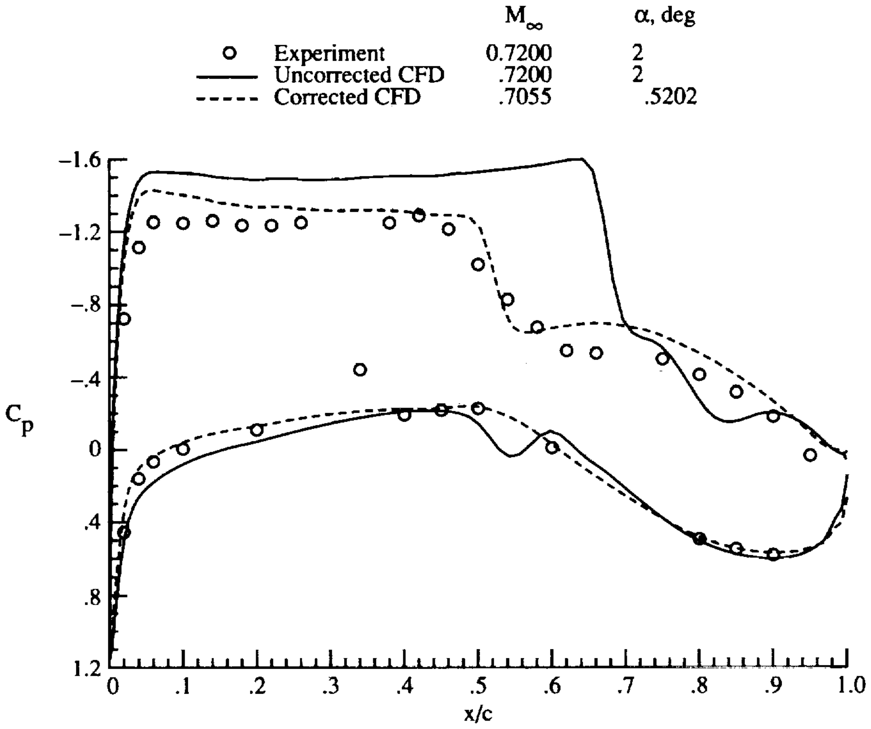

Figure 18. Effect of Mach number and angle-of-attack corrections at $R_c = 35 \times 10^6$.

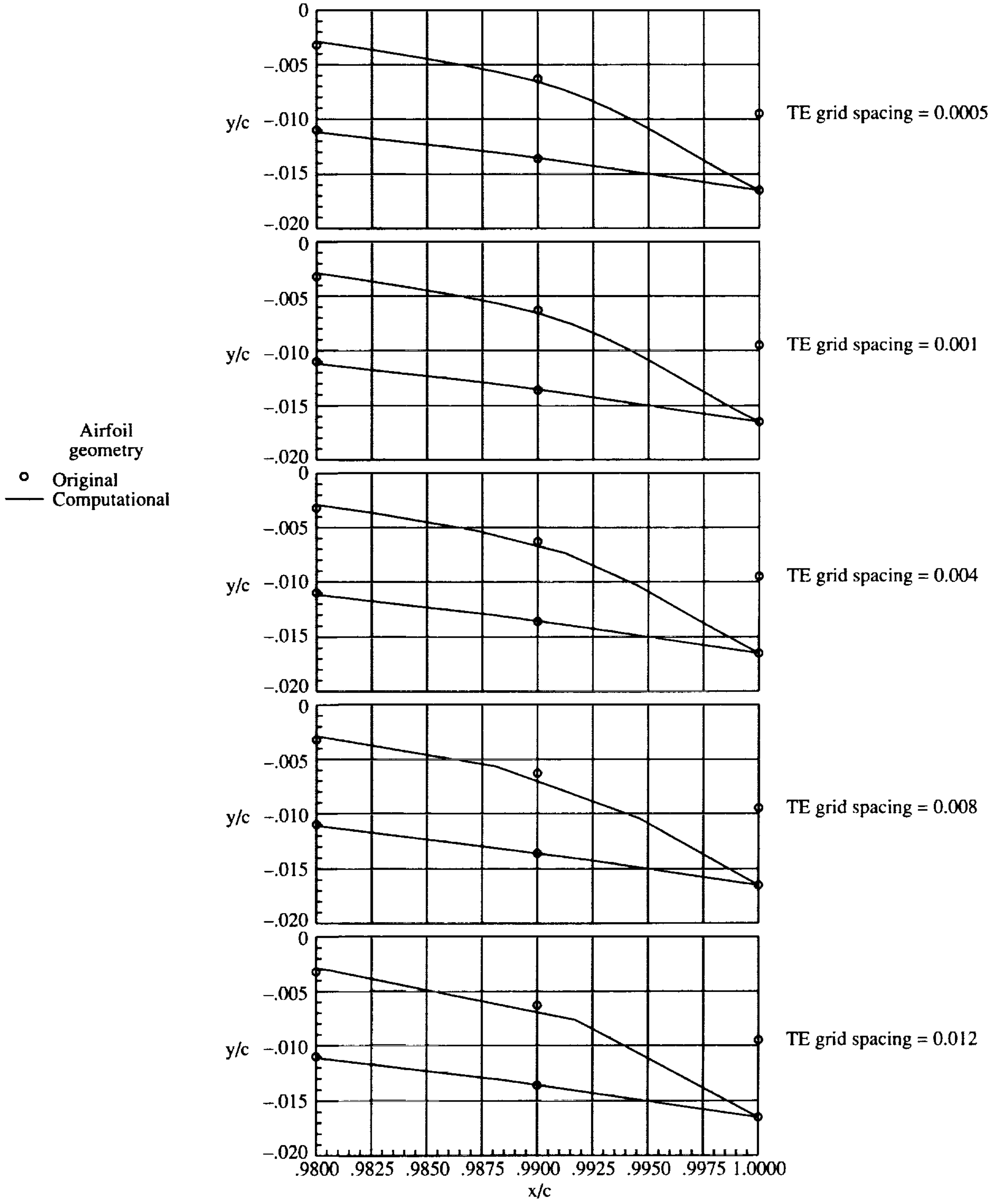

Figure 19. Original geometry (table 1) compared with computational surfaces.

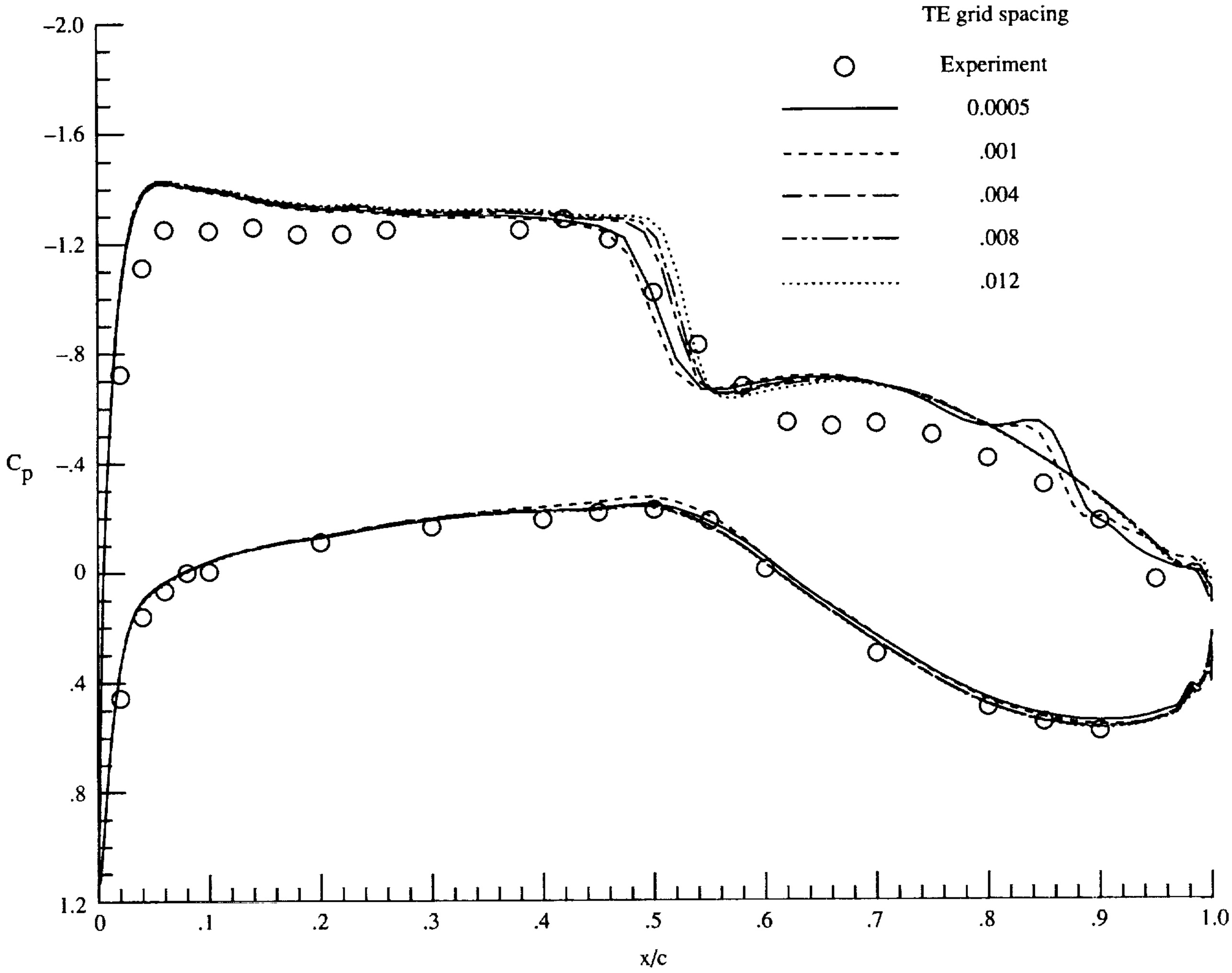

Figure 20. Computational results showing effect of trailing-edge spacing with final trailing-edge closure. $R_c = 35 \times 10^6$; $M_{\infty,c} = 0.7055$; $\alpha_c = 0.5202°$.

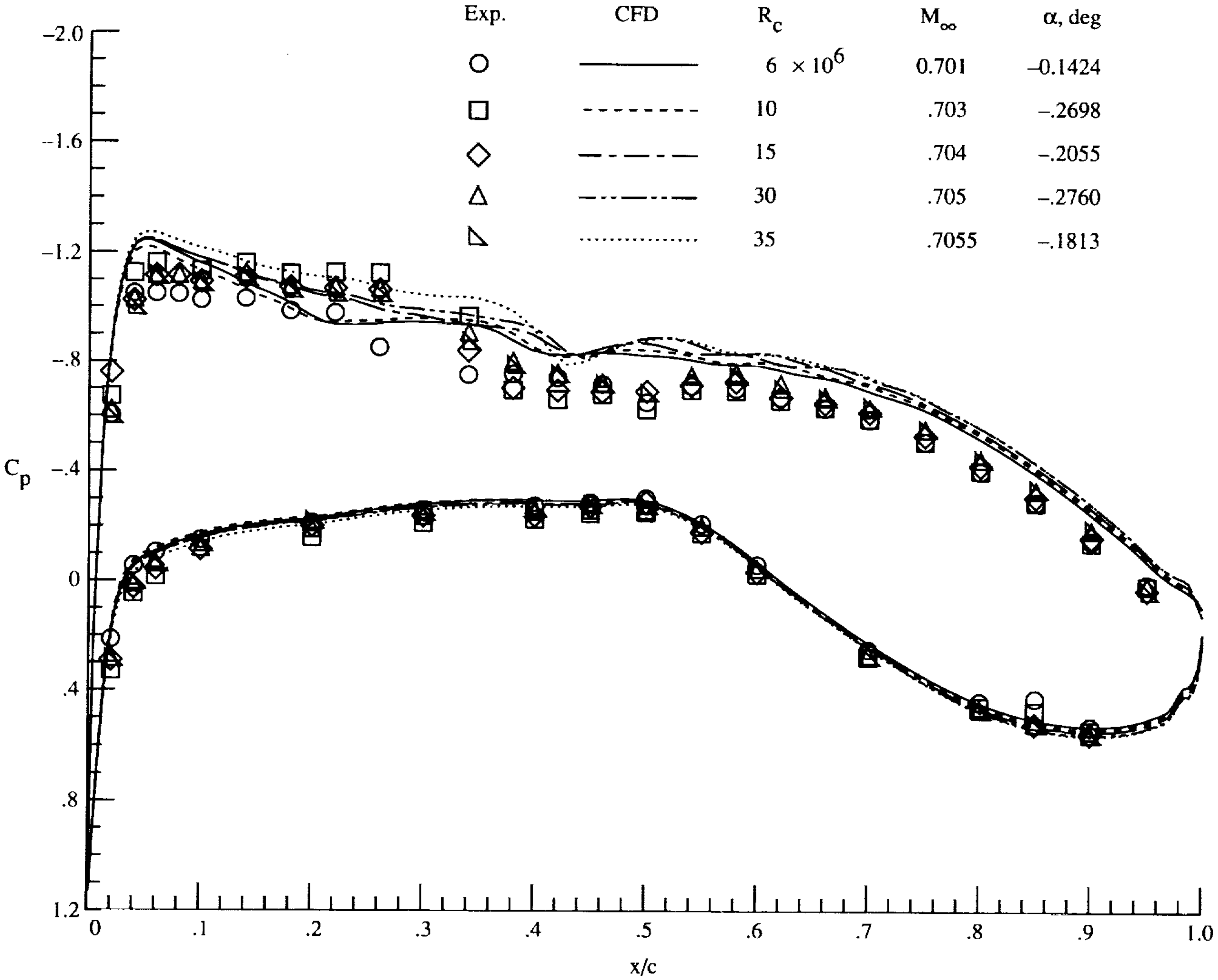

Figure 21. Reynolds number effects at $M_{\infty,\mathrm{un}} = 0.72$ and $\alpha_{\mathrm{un}} = 1°$.

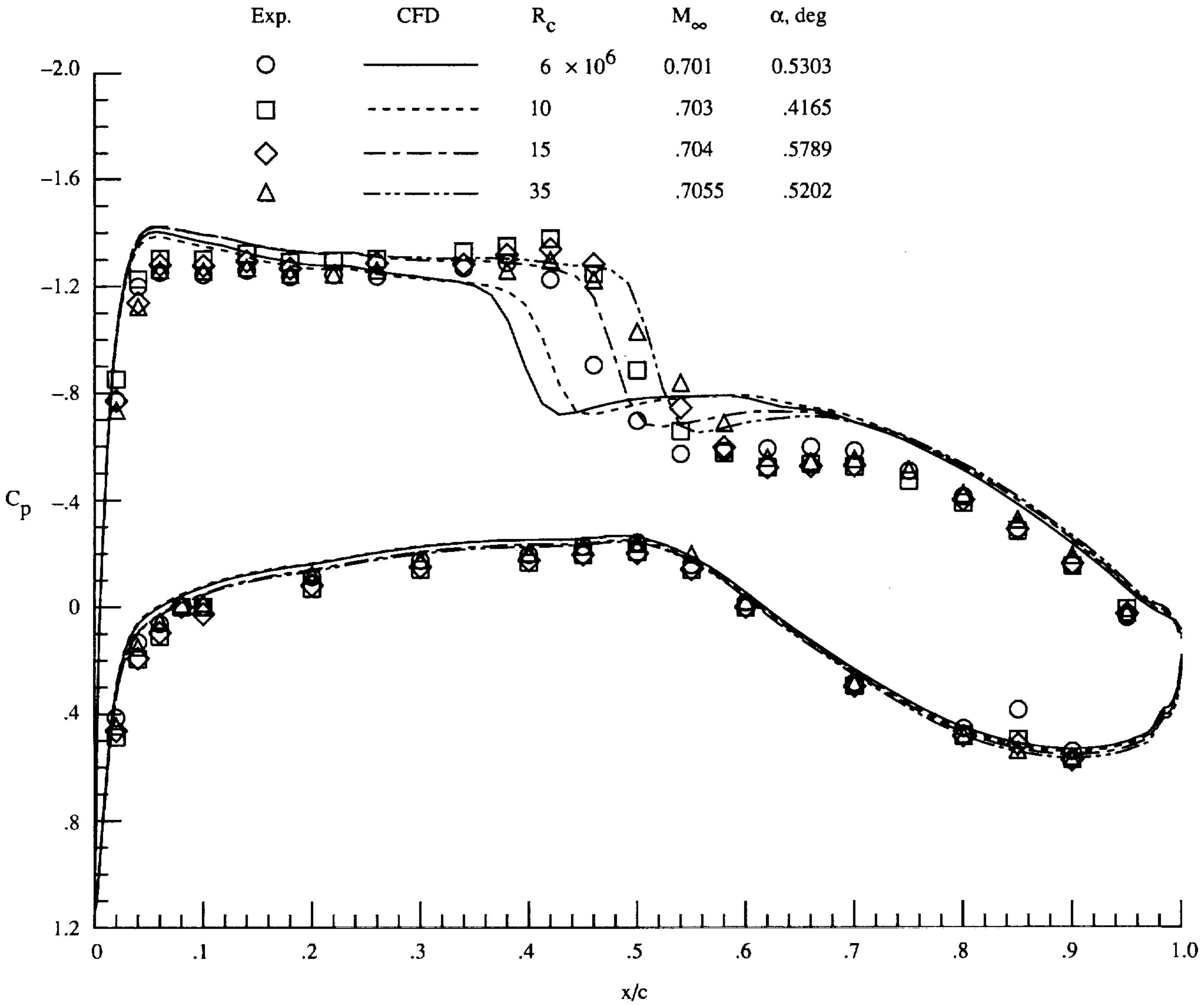

Figure 22. Reynolds number effects at $M_{\infty,\mathrm{un}} = 0.72$ and $\alpha_{\mathrm{un}} = 2°$.

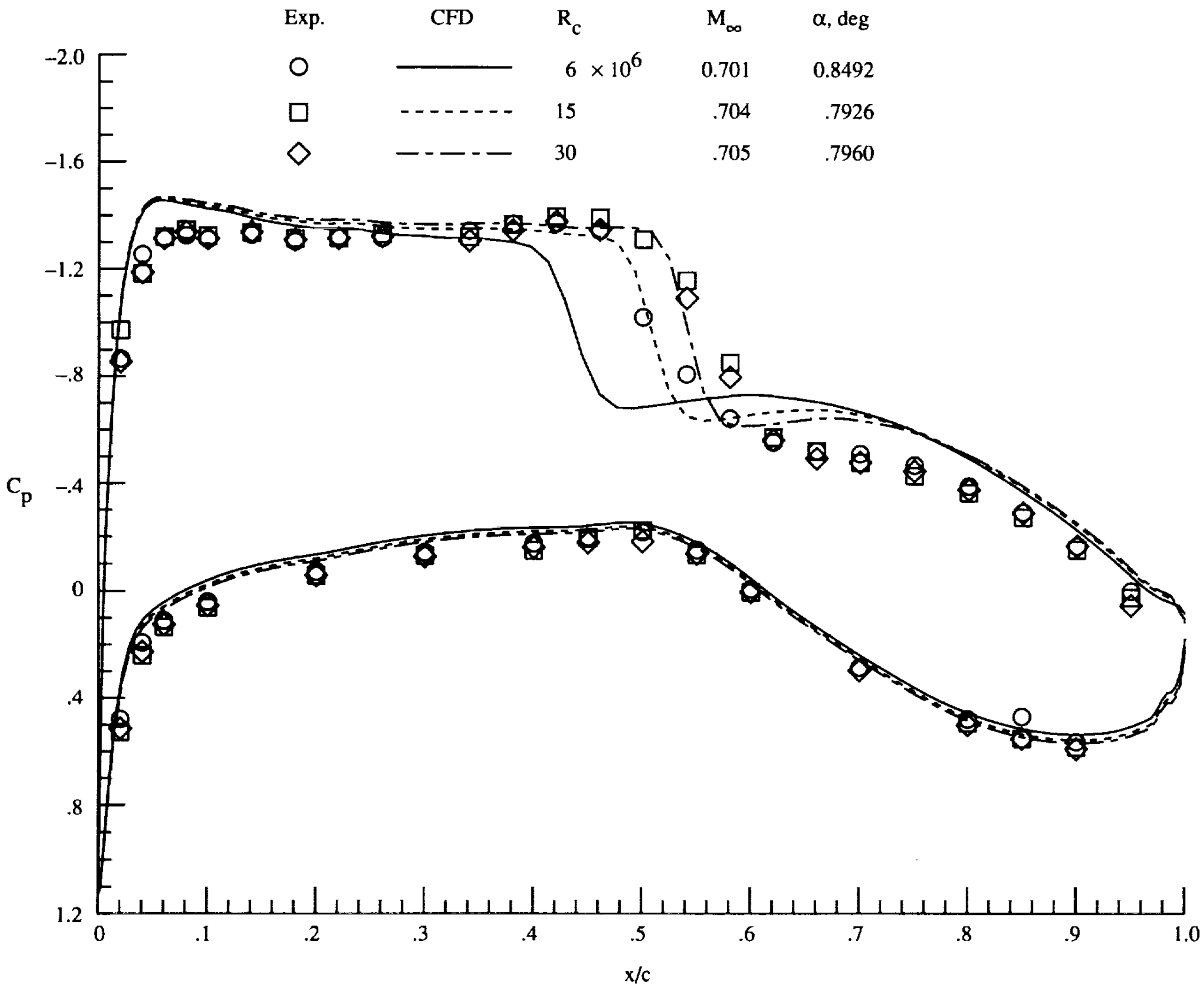

Figure 23. Reynolds number effects at $M_{\infty,\mathrm{un}} = 0.72$ and $\alpha_{\mathrm{un}} = 2.5°$.

REPORT DOCUMENTATION PAGE

Form Approved
OMB No. 0704-0188

Public reporting burden for this collection of information is estimated to average 1 hour per response, including the time for reviewing instructions, searching existing data sources, gathering and maintaining the data needed, and completing and reviewing the collection of information. Send comments regarding this burden estimate or any other aspect of this collection of information, including suggestions for reducing this burden, to Washington Headquarters Services, Directorate for Information Operations and Reports, 1215 Jefferson Davis Highway, Suite 1204, Arlington, VA 22202-4302, and to the Office of Management and Budget, Paperwork Reduction Project (0704-0188), Washington, DC 20503.

1. AGENCY USE ONLY*(Leave blank)*

2. REPORT DATE
November 1994

3. REPORT TYPE AND DATES COVERED
Technical Memorandum

4. TITLE AND SUBTITLE
Comparison of Computational and Experimental Results for a Supercritical Airfoil

5. FUNDING NUMBERS
WU 505-59-10-31

6. AUTHOR(S)
Melissa B. Rivers and Richard A. Wahls

7. PERFORMING ORGANIZATION NAME(S) AND ADDRESS(ES)
NASA Langley Research Center
Hampton, VA 23681-0001

8. PERFORMING ORGANIZATION REPORT NUMBER
L-17320

9. SPONSORING/MONITORING AGENCY NAME(S) AND ADDRESS(ES)
National Aeronautics and Space Administration
Washington, DC 20546-0001

10. SPONSORING/MONITORING AGENCY REPORT NUMBER
NASA TM-4601

11. SUPPLEMENTARY NOTES

12a. DISTRIBUTION/AVAILABILITY STATEMENT
Unclassified–Unlimited
Subject Category 02
Availability: NASA CASI (301) 621-0390

12b. DISTRIBUTION CODE

13. ABSTRACT *(Maximum 200 words)*

A computational investigation was performed to study the flow over a supercritical airfoil model. Solutions were obtained for steady-state transonic flow conditions using a thin-layer Navier-Stokes flow solver. The results from this computational study were compared with time-averaged experimental data obtained over a wide Reynolds number range at transonic speeds in the Langley 0.3-Meter Transonic Cryogenic Tunnel. Comparisons were made at a nominal Mach number of 0.72 and at Reynolds numbers ranging from 6×10^6 to 35×10^6.

14. SUBJECT TERMS
Steady flow; Computational fluid dynamics; Supercritical airfoil; Reynolds number effects; Cryogenic wind tunnel

15. NUMBER OF PAGES
27

16. PRICE CODE
A03

17. SECURITY CLASSIFICATION OF REPORT
Unclassified

18. SECURITY CLASSIFICATION OF THIS PAGE
Unclassified

19. SECURITY CLASSIFICATION OF ABSTRACT
Unclassified

20. LIMITATION OF ABSTRACT

NSN 7540-01-280-5500

Standard Form 298(Rev. 2-89)
Prescribed by ANSI Std. Z39-18
298-102